Design of intrinsically disordered proteins that undergo phase transitions with lower critical solution temperatures

Xiangze Zeng[1], Chengwen Liu[2], Martin J. Fossat[1], Pengyu Ren[2], Ashutosh Chilkoti[3], Rohit V. Pappu[1*]

[1]Department of Biomedical Engineering and Center for Science & Engineering of Living Systems (CSELS), Washington University in St. Louis, St. Louis, MO 63130, USA

[2]Department of Biomedical Engineering, The University of Texas at Austin, Austin, TX 78712, USA

[3]Department of Biomedical Engineering, Duke University, Durham, NC 27708, USA

*Corresponding author: pappu@wustl.edu

Abstract

Many naturally occurring elastomers are intrinsically disordered proteins (IDPs) built up of repeating units and they can demonstrate two types of thermoresponsive phase behavior. Systems characterized by lower critical solution temperatures (LCST) undergo phase separation above the LCST whereas systems characterized by upper critical solution temperatures (UCST) undergo phase separation below the UCST. There is congruence between thermoresponsive coil-globule transitions and phase behavior. Specifically, the theta temperatures above or below which the IDPs transition from coils to globules serve as useful proxies for the LCST / UCST values. This implies that one can design sequences with desired values for the theta temperature with either increasing (UCST) or decreasing radii of gyration (LCST) above the theta temperature. Here, we show that the Monte Carlo simulations performed in the so-called intrinsic solvation (IS) limit version of the temperature-dependent ABSINTH implicit solvation model, yields a robust heuristic for discriminating between sequences with known LCST versus UCST phase behavior. Accordingly, we use this heuristic in a supervised approach, integrate it with a genetic algorithm, combine this with IS limit simulations, and show how novel sequences can be designed that have LCST phase behavior. These calculations are aided by direct estimates of temperature dependent free energies of solvation for model compounds that are derived using the polarizable AMOEBA forcefield. To demonstrate the validity of our designs, we calculate coil-globule transition profiles using the full ABSINTH model and combine these with the Gaussian Cluster Theory to show that the designed IDPs do show LCST phase behavior.

Introduction

Intrinsically disordered proteins (IDPs) that undergo thermoresponsive phase transitions are the basis of many naturally occurring elastomeric materials [1]. These naturally occurring

scaffold IDPs [2] serve as the basis of ongoing design efforts to design thermoresponsive materials [3]. Well-known examples of disordered regions derived from elastomeric proteins [4], include the repetitive sequences from proteins such as resilins [5], elastins [6], proteins from spider silks [7], titin [8], and neurofilament sidearms [9]. Elastin-like polypeptides have served as the benchmark systems for the development of responsive disordered proteins that can be adapted for use in various biotechnology settings [10]. The interplay between sequence-encoded intermolecular and chain-solvent interactions combined with the interplay between chain and solvent entropy gives rise to thermoresponsive phase transitions that lead to the formation of coacervates [1]. Here, we show that one can expand the "materials genome" [11] through *de novo* design strategies that are based on heuristics anchored in the physics of thermoresponsive transitions and efficient simulation engines that apply the learned heuristics in a supervised approach. We report the development of a genetic algorithm (GA) and show how it can be applied in conjunction with multiscale computations to design thermoresponsive IDPs with LCST phase behavior.

Conformational heterogeneity is a defining hallmark of IDPs [12]. Work over the past decade-and-a-half has shown that naturally occurring IDPs come in distinct sequence flavors [12]. Indeed, IDPs can be distinguished based on their sequence-encoded interplay between intramolecular and chain-solvent interactions that can be altered through changes in solution conditions. Recent studies have shown that IDPs can be drivers or regulators of reversible phase transitions in simple and complex mixtures of protein and nucleic acid molecules [13]. These transitions are driven primarily by the multivalence of interaction motifs that engage in reversible physical crosslinks [14]. IDPs can serve as scaffolds for interaction motifs (stickers), interspersed by spacers. Alternatively, they can modulate multivalent interactions mediated by stickers that are situated on the surfaces [15] of autonomously foldable protein domains [16].

Thermoresponsive phase transitions arise either by increasing the solution temperature above a lower critical solution temperature (LCST) or by lowering the temperature below an upper critical solution temperature (UCST) [1]. Many systems are capable of both types of thermoresponsive transitions, although only one of the transitions might be accessible in the temperature range of interest. Here, we leverage our working knowledge of the sequence features that encode driving forces for thermoresponsive phase transitions [17] to develop and deploy a GA for the design of novel IDPs characterized by LCST behavior. Inspired by work on elastin-like polypeptides [3], we focus on designing IDPs that are repeats of pentapeptide motifs. The amino acid composition of each motif contributes to the LCST behavior and the number of repeats determines the multivalence of stickers that drive phase transitions with LCST behavior.

The GA we adapt for this work is driven by advances that include: (a) an improved fundamental understanding of the physics of LCST phase behavior [18]; (b) experiments showing that many IDPs undergo collapse transitions with increased temperature [19]; (c) a generalization of the ABSINTH implicit solvation model and forcefield paradigm[20] to account for the temperature dependence of chain solvation; (d) a growing corpus of information regarding the sequence determinants of LCST phase behavior in repetitive IDPs [17]; and (e) the prior demonstration that a GA based method known as GADIS [21] can be combined with efficient, ABSINTH-based simulations to design IDPs with bespoke secondary structural preferences.

Studies of synthetic polymer systems have helped in elucidating the origins of the driving forces for and the mechanisms of LCST phase behavior [22]. A well-known example is poly-N-isopropylacrylamide (PNIPAM) [23]. Here, the dispersed single phase is stabilized at temperatures below ~32˚C by the favorable hydration of amides in the sidechains. Solvation of amides requires that the solvent be organized around the hydrophobic moieties that include the backbone carbon

chain and the isopropyl group in the sidechain. The entropic cost for organizing solvent molecules around individual chains increases with increasing temperature. Accordingly, above the LCST of ~32˚C, and for volume fractions that are greater than a threshold value, the system phase separates to form a polymer-rich coacervate phase that coexists with a polymer-poor dilute phase. The driving forces for phase separation are the gain in solvent entropy through the release of solvent molecules from the polymer and the gain of favorable inter-chain interactions, such as hydrogen-bonding interactions between amides in the polymer.

Tanaka and coworkers have developed a *cooperative hydration* approach, inspired by the Zimm and Bragg theories for helix-coil transitions [24], to model the physics of phase transitions with LCST [25]. Cooperative hydration refers to the cooperative association (below the LCST) or dissociation (above the LCST) of water molecules that are bound to repeating units along the polymer chain [26]. Cooperativity is captured using the Zimm-Bragg formalism by modeling each repeating unit as being in one of two states *viz*., solvated or desolvated. In the solvated state, the repeating unit has a defined interaction strength with solvent molecules. In the desolvate state, pairs of such repeating units have defined exchange interactions. In addition, desolvation is associated with a gain in solvent entropy. The three-way interplay of direct solvent-chain interactions, the interactions among desolvated pairs of units, and the gain in solvent entropy above the LCST can be captured in a suitable physical framework that can be parameterized to describe system-specific phase transitions. Accordingly, if one has prior knowledge of the interaction energies associated with each repeat unit, one can use the framework of Tanaka and coworkers to design novel sequences with LCST behavior.

An alternative approach, which we adopt in this work, is to leverage the corollary of LCST behavior at the single chain limit [27]. At temperatures that are proximal to the LCST, the system of

chain of interest will undergo a coil-to-globule transition in a dilute solution [28]. This is because the chain collapse is a manifestation of the physics of phase separation at the single chain limit. Here, we leverage this connection between phase separation and chain collapse of isolated polymer chains in ultra-dilute solutions to design novel IDPs that are predicted to undergo phase transitions with LCST phase behavior. To do so by using a multi-pronged approach that starts with improved estimates of the temperature dependencies of free energies of solvation of model compounds that mimic amino acid sidechain and backbone moieties. For this, we use free energy calculations based on the AMOEBA forcefield [29], which is built on a second-generation polarizable model for water molecules and proteins. We incorporate these temperature dependent free energies of solvation into the ABSINTH implicit solvation model and show that thermoresponsive changes to chain dimensions, calculated in the efficient "*intrinsic solvation* (IS) limit" [30] yields robust heuristics that discriminates sequences with known LCST phase behavior from those that show UCST behavior. We then describe the development of a GA, an adaptation of the GADIS approach, to design novel sequences that relies on all-atom simulations, performed using the ABSINTH model in the IS limit, and learned heuristics as fitness scores. We show that distinct classes of designed sequences emerge from our approach. These are screened to filter out sequences with low disorder scores as assessed using the IUPRED2 algorithm [31]. The resulting set of sequences are analyzed using simulations based on the full ABSINTH model, which show that the designed sequences do undergo collapse transitions above a threshold temperature. The contraction ratio, defined as the ratio of chain dimensions at temperature T to the dimensions at the theta temperature, is computed as a function of simulation temperature is analyzed to extract temperature dependent two-body interaction parameters and athermal three-body interaction parameters that are used in conjunction with the Gaussian Cluster Theory (GCT) [32] to calculate system-specific phase diagrams [28]. The

upshot is multiscale pipeline whereby a GA, aided by supervised learning in the form of a derived heuristic and IS limit simulations, leads to the design of novel sequences with predicted LCST phase behavior. Following a post-processing step that selects for sequences with a high confidence of being intrinsically disordered, we combine all-atom ABSINTH-T based simulations with Gaussian Cluster Theory to obtain sequence-specific phase diagrams. These last two steps allow further pruning of the sequence space derived from the designs and provide further confidence regarding the authenticity of the predicted LCST phase behavior.

Results and Discussion

Temperature dependent free energies of hydration for model compound mimics of backbone and sidechain moieties of proteins

Preamble: LCST phase behavior is determined by the temperature dependent free energies of hydration ($\Delta\mu_h$) of protein solutes. Each protein may be viewed as a chain of model compounds and measured / calculated temperature dependent values of $\Delta\mu_h$ for fully solvated model compounds can be used as the reference free energy of solvation (rFoS) in implicit solvation models such as EEF1[33] or ABSINTH [20]. In these computational approaches, the rFoS of each model compound is modulated by alterations to their local environments through conformational changes. We use the ABSINTH implicit solvation model [20] and forcefield paradigm [34] to model the linkage between conformational equilibria and solvent-mediated interactions among polypeptide atoms. This allows us to perform simulations of temperature dependent coil-to-globule transitions, extract parameters to the Gaussian cluster theory [32], and deploy these parameters in numerical calculations to generate full phase diagrams for the IDP of interest [28]. Accordingly, rFoS values of model compound mimics of sidechain and backbone moieties are key parameters that

drive ABSINTH-based simulations of temperature dependent collapse of individual IDPs in dilute solutions as well as the calculation of phase diagrams.

Wuttke et al.,[19] incorporated temperature dependent rFoS values into ABSINTH to model the collapse transition observed experimentally for different IDPs. To calculate temperature dependent rFoS values, Wuttke et al. used data from measurements made by Makhatadze and Privalov [35] for the enthalpy and heat capacity of hydration at a reference temperature. These values were then incorporated into the integrated version of the Gibbs-Helmholtz equation to yield a thermodynamic model for temperature dependent rFoS values for all the relevant model compounds. In this formalism, rFoS(T) or $\Delta\mu_h(T)$ is written as:

$$\Delta\mu_{\mathrm{h}}\left(T\right)=\frac{\left[\Delta\mu_{\mathrm{h}}\left(T_0\right)-\Delta h\right]T}{T_0}+\Delta h+\Delta c_P\left[T\left(1-\ln\frac{T}{T_0}\right)-T_0\right]; \quad (1)$$

Here, Δh is the enthalpy of solvation at a reference temperature T_0, which is typically set to be 298K, and Δc_P is the molar heat capacity change associated with the solvation process. For simplicity, this is assumed to be independent of temperature [36].

We build on the approach of Wuttke et al., which leverages the flexibility of the ABSINTH model, wherein the temperature dependence of solvation properties can be modeled by incorporating temperature dependent rFoS values in ABSINTH. This leads to a version of ABSINTH that we refer to here as ABSINTH-T. However, instead of relying on extrapolations based on measurements at single temperatures and the integral of the Gibbs-Helmholtz equation, we directly calculate the temperature dependence of rFoS values using free energy simulations performed at different temperatures using the polarizable AMOEBA forcefield [29] for model compounds and water. With these values in hand, we obtain parameters for the integral of the

Gibbs-Helmholtz equation, which we then use in ABSINTH-T based simulations to design novel sequences that are predicted to show LCST behavior. Direct calculations of free energies of solvation obviate the need for making *a priori* assumptions when using experimentally derived values, which become especially problematic for model compounds with ionizable groups.

Results from AMOEBA-based free energy calculations for model compounds: We performed temperature dependent free energy calculations based on the Bennett Acceptance Ratio (BAR) free energy estimator [37] for direct investigation of how $\Delta\mu_h$ varies with temperature. These calculations were performed for nineteen different model compounds that mimic the twenty sidechain moieties and the backbone peptide unit. For the free energy calculations, we used the AMOEBA forcefield, which uses atomic polarizabilities and atom-centered multipoles up to quadrupole moments [29]. The AMOEBA forcefield represents the state-of-the-art in modeling protein and peptide units in aqueous solutions using polarizability and higher-order electrostatics without having to resort to quantum mechanical calculations. Importantly, the AMOEBA water model reproduces the temperature-dependent anomalies of liquid water [38] a feature that is directly relevant for extracting temperature-dependent parameters to describe solvation. Additionally, the AMOEBA model yields accurate free energies of solvation of ions [39] and model compounds in aqueous solvents [29,38,40]. Details of the parameterization for model compounds used in this study, and the design of the free energy calculations are provided in the methods section.

Results from temperature dependent calculations of μ_h for the nineteen relevant model compounds are shown in **Figure 1**. These panels are grouped by the chemistries of functional groups within the different model compounds. The enthalpy of hydration (Δh) at T_0 = 298K and the temperature independent heat capacities of hydration (Δc_P) were extracted for each model

compound by fitting the calculated temperature dependent free energies of solvation to the integral of the Gibbs-Helmholtz equation – see equation (1). The results are summarized in **Table 1**.

As expected for hydrophobic hydration [36], the large positive heat capacity of hydration combined with the favorable enthalpies and unfavorable entropies lead to non-monotonic temperature dependencies for model compound mimics of the sidechain moieties of Ala, Val, Leu, Ile, and Pro. Similar results are observed for mimics of Phe, Tyr, and Trp. The two striking observations are the differences in hydration thermodynamics of the model compounds that mimic sidechains of Lys, Arg, Asp, and Glu. The model compounds 1-butylamine and *n*-propylguanidine that mimic the sidechains of Lys and Arg, respectively, have a bipartite character. Favorable interactions of water molecules with the amine and guanidinium groups of Lys and Arg are offset by unfavorable hydration of the alkyl portions of these sidechains. This leads to a duality of favorable enthalpy of hydration and large positive values for Δc_P. The highly favorable enthalpy gives rise to large negative values for μ_h, whereas the entropic cost of hydration causes a decrease in the favorability of hydration as temperature increases. This is especially true for the mimic of Arg, which has a large negative enthalpy of hydration and a large positive heat capacity of hydration that is equivalent to that of hydrocarbon mimics of hydrophobic sidechains. The patterns for Lys are similar, although the heat capacity of hydration is a third of that of the Arg sidechain. The differences in heat capacities and temperature dependencies of free energies of hydration start to provide a rationalization for many of the recent observations reported in the literature. Recent studies have shown that Lys and Arg are not interoperable as equivalent replacements in polyampholytic IDPs [41], synthetic systems that drive phase separation [42], and natively occurring drivers of phase separation including RNA binding domains [43], and components of nuclear speckles [44].

Finally, the deprotonated versions of acetic acid and propionic acid that mimic the deprotonated versions of Asp and Glu, respectively, have the most favorable free energies of hydration across the temperature range studied. This originates in the highly favorable enthalpy of hydration. Interestingly, these two solutes stand out for their distinctive negative heat capacities of hydration. Inferences based on integral equation theories [45] suggest that negative heat capacities of hydration derive from a weakening of the favorable solute-solvent interactions and a reduction of the extent to which water molecules are orientationally distorted within and in the vicinity of the first hydration shell. These thermodynamic assessments suggest that the negative heat capacities of hydration might be responsible for the observed deficiency of acidic groups, specifically Asp sidechains in sequences that undergo LCST behavior [1].

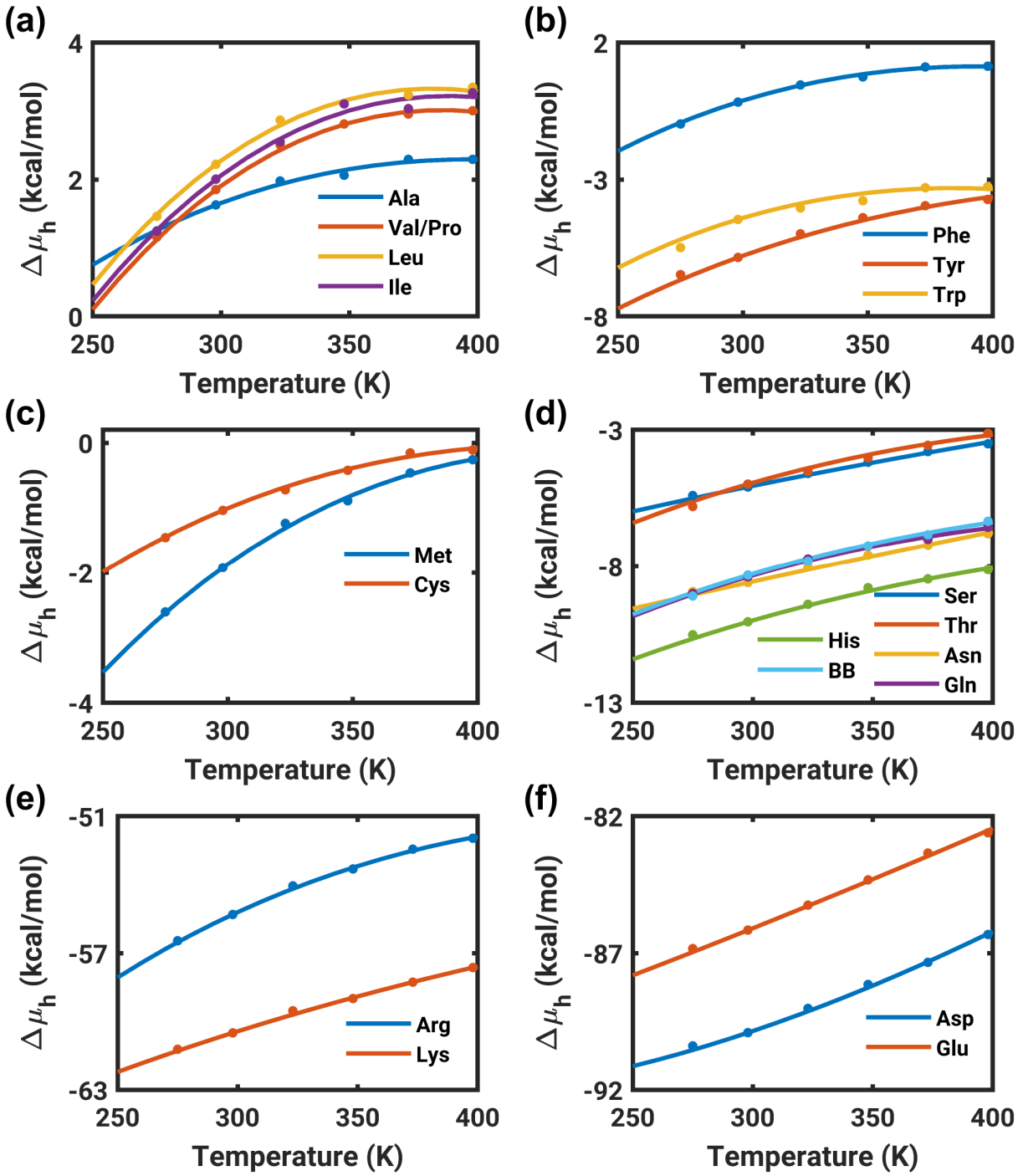

Figure 1: Temperature dependent free energies of solvation $\Delta\mu_h$ for model compounds that mimic sidechain and backbone moieties. The dots show results from free energy calculations based on the AMOEBA forcefield. These values are then fit to the integral of the Gibbs-Helmholtz equation (see main text) and the results of the fits are shown as solid curves. Parameters from the fits, which include estimates for Δh and Δc_P are shown in **Table 1**. In the legends we use the three letter abbreviations for each of the amino acids. Here, BB in panel (d) refers to the backbone moiety, modeled using N-methylacetamide, that mimics the peptide unit.

Table 1: Results from free energy calculations that summarize values obtained for $\Delta\mu_h$ at 298 K. Data for the temperature dependence of $\Delta\mu_h$ were fit to equation (1), setting T_0 = 298 K, to extract values for Δh and Δc_P.

Residue / unit	Model compound	$\Delta\mu_h$ kcal/mol	Δh kcal/mol	Δc_P cal / mol-K
Ala	methane	1.63	-2.57	48.93
Val / Pro	propane	1.85	-6.33	105.80
Leu	2-methalpropane	2.22	-5.92	109.38
Ile	*n*-butane	2.00	-6.34	105.23
Met	ethyl methyl thioether	-1.92	-10.11	71.10
Phe	toluene	-0.17	-8.68	102.24
Cys	methanethiol	-1.04	-5.84	43.61
Tyr	p-Cresol	-5.85	-15.62	71.09
Trp	3-Methylindole	-4.46	-12.67	108.10
Ser	methanol	-5.08	-10.41	10.43
Thr	ethanol	-4.98	-12.55	50.06
Asn	acetamide	-8.61	-14.37	6.18
Gln	propionamide	-8.39	-16.06	51.47
His	4-methylimidazole	-10.04	-17.60	38.01
backbone / Gly	N-methylacetamide	-8.33	-16.10	44.73
Arg	*n*-propylguanidine	-55.30*	-69.91	101.02
Lys	1-butylamine	-60.49*	-70.37	29.98
Asp	acetic acid	-89.91*	-98.65	-44.97
Glu	propionic acid	-86.16*	-96.62	-8.75

*As with the default ABSINTH model, in ABSINTH-T, the rFoS values we used for ionizable residues are offset from the calculated $\Delta\mu_h$ by a fixed constant of -30 kcal/mol. This, as was shown in the original work, is required to avoid the chelation of solution ions around ionizable residues. This "feature" remains a continuing weakness of the ABSINTH paradigm and one that we hope to remedy through suitable generalization of the model used in ABSINTH to interpolate between fully solvated and fully desolvated states.

Incorporation of T-dependent rFoS values into ABSINTH: In the ABSINTH model, each polyatomic solute is parsed into a set of solvation groups [20,46]. These groups are model compounds for which the free energies of solvation rFoS are known *a priori*. In this work, we follow Wuttke et al.,[19] and generalize the ABSINTH model to incorporate temperature dependencies of model compound rFoS values. In this ABSINTH-T model, the total solvent-mediated energy associated for a given configuration of the protein and solution ions is written as:

$$E_{\text{total}} = W_{\text{solv}}(T) + W_{\text{el}}(T) + U_{\text{LJ}} + U_{\text{corr}}\,; \tag{2}$$

Here, $W_{\text{solv}}(\{\text{rFoS}(T)\},\{\mathbf{r}\})$ is the many-body direct mean field interaction (DMFI) with the continuum solvent that depends on $\{\text{rFoS}(T)\}$, the set of temperature dependent rFoS values of model compounds that make up the solute and solution ions, and $\{\mathbf{r}\}$ is the set of configurational coordinates for polypeptide atoms and solution ions. The term $W_{\text{solv}}(\{\text{rFoS}(T)\},\{\mathbf{r}\})$quantifies the free energy change associated with transferring the polyatomic solute into a mean field solvent while accounting for the temperature dependent modulation of the reference free energy of solvation for each solvation group due to other groups of the polyatomic solute as well as the solution ions. Additional modulations to the free energy of solvation of the solute due to interactions with charged sites on the polyatomic solute are accounted for by the W_{el} term. In ABSINTH-T the term $W_{\text{el}}(\{\mathbf{r}\},\{\upsilon\},\varepsilon(T))$ is a function of the set of configurational coordinates $\{\mathbf{r}\}$and solvation states $\{\upsilon\}$ of the solute atoms and solution ions, and the temperature dependent dielectric constant $\varepsilon(T)$. For $\varepsilon(T)$, we used the parameterization of Wuttke et al., [19]. The effects of dielectric inhomogeneities, which are reflected in the configuration dependent solvation states, are accounted for without making explicit assumptions regarding the distance or spatial dependencies of dielectric saturation. The term U_{LJ} is a standard 12-6 Lennard-Jones potential and U_{corr} models specific torsion and bond angle-dependent stereoelectronic effects that are not captured by the U_{LJ} term. The ABSINTH paradigm is optimally interoperable with the OPLS-AA/L and the CHARMM [47] family of forcefields, and we use the OPLS-AA/L [48] forcefield.

Intrinsic solvation (IS) model, a non-electrostatics version of ABSINTH-T as an efficient heuristic for discriminating IDPs with LCST versus UCST behavior

In the single chain limit, accessible in dilute solutions, polypeptides that show LCST phase behavior undergo collapse above a system specific theta temperature, whereas polypeptides that show UCST phase behavior expand above the system specific theta temperature [1,28]. A GADIS-like strategy [21] for *de novo* design of polypeptide sequences with LCST phase behavior would involve ABSINTH-T based all-atom simulations to evaluate whether an increase in temperature leads to chain collapse. In effect, the fitness function in a GA comes from evaluation of the simulated ensembles as a function of temperature. This becomes prohibitively expensive computationally. Accordingly, we pursued a pared down version of ABSINTH-T, which is referred to as the intrinsic solvation (IS) limit of the model [30]. The IS limit was introduced to set up sequence and composition specific reference models with respect to which one can use mean-field models to uncover how desolvation impacts IDP ensembles [30,49]. In effect, the IS limit helps us map conformations in the maximally solvated ensemble and assess how this ensemble changes as a function of temperature. In the IS limit, the energy in a specific configuration for the sequence of interest is written as:

$$E_{\text{IS-limit}} = W_{\text{solv}}(T) + U_{\text{LJ}} + U_{\text{corr}}; \tag{3}$$

The only difference between the full model, see equation (2), and the IS limit is the omission of the W_{el} term. This increases the speed of simulations by roughly two orders of magnitude. Next, we asked if ensembles obtained from temperature dependent simulations performed in the IS limit could be used to obtain a suitable heuristic that discriminates sequences with LCST versus UCST behavior. These simulations were performed for a set of thirty sequences (see **Table S1**) that were previously shown by Garcia Quiroz and Chilkoti to have LCST and UCST phase behavior [17]. The results are summarized in **Figure 2**. As shown in panel (a) of **Figure 2**, the radii of gyration (R_g), suitably normalized for comparisons across different sequences of

different lengths, appear to be segregated into two distinct classes. To test this hypothesis, we computed the slopes m for each of the profiles of normalized R_g versus temperature. These slopes were calculated in the interval of simulation temperatures between 230 K and 380 K. The results are shown in panel (b) of **Figure 2**. These data show that there indeed are two categories of sequences. Those that are known to show LCST phase behavior are colored in red, and they fall into distinct group characterized by negative values of the slope m with an average value of -5.9×10^{-3} åK^{-1}. Here, we use å to denote the units of R_g values normalized by the square root of the chain length N. In contrast, the slope for sequences that show UCST behavior is -1.4×10^{-3} åK^{-1}. Given the range of sequences covered in the calibration based on the IS limit, we pursued an approach whereby we use slopes of $R_g N^{-0.5}$ vs. T as a heuristic to guide the design of a genetic algorithm to find new sequences with LCST phase behavior.

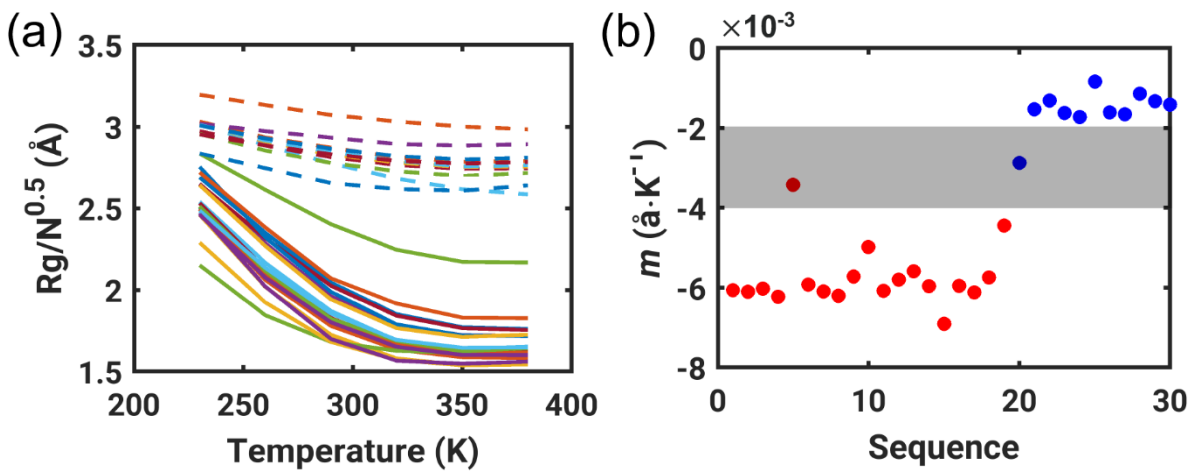

Figure 2: Analysis of IS limit simulations yields a heuristic that discriminates sequences with UCST vs. LCST phase behavior. (a) Plots of $R_g N^{0.5}$ vs. temperature, extracted from IS limit simulations, for sequences shown by Garcia Quiroz and Chilkoti to have UCST (dashed lines) vs. LCST (solid lines) phase behavior. The sequences are shown in **Table S1** in the supporting information. (b) The slope m of the $R_g N^{0.5}$ vs. temperature profiles. These slopes fall into two distinct categories, one for those with LCST phase behavior (blue) and another for those with UCST phase behavior (red). The gray region corresponds to the values of m that clearly demarcate the two categories of sequences.

GA for the design of IDPs that are likely to have LCST phase behavior

Motivated by previous successes using the GADIS algorithm [21] for designing sequences with bespoke amounts of intrinsic secondary structure contents, we adapted a GA for exploring sequence space to discover candidate IDPs with predicted LCST phase behavior. To introduce the GA and demonstrate its usage, we set about designing novel sequences that are repeats of pentapeptide motifs. We focused on designing 55-mers, i.e., sequences with 11 pentapeptides. To keep the exercise simple, we focused on designing polymers that are perfect repeats of the pentapeptide in question. The GA used in this work is summarized in **Figure 3** and the details are described below.

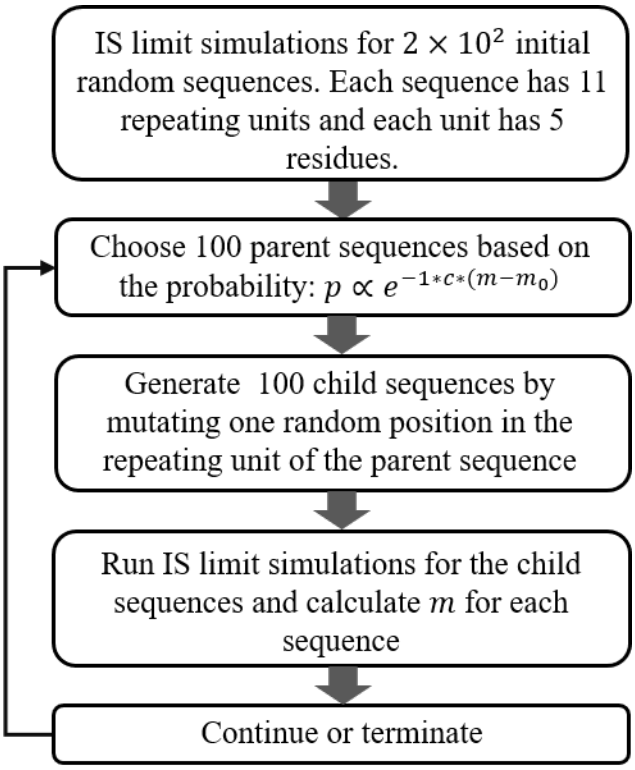

Figure 3. Workflow of the GA. We use this approach to design sequences that are predicted to have LCST phase behavior. A final post-processing step is added to filter our sequences that do not have high disorder scores (see main text).

The GA based design process is initiated by choosing a random set of 200 sequences. Next, for each of the random sequences we performed temperature based replica exchange [50] Metropolis Monte Carlo simulations in the IS limit. Details of these simulations are described in the methods section. The simulation temperatures range from 200 K to 375 K with an interval of 25 K. From each converged IS limit simulation we computed the ensemble averaged R_g values as a function of simulation temperature T. These data were then used to evaluate the initial set of 200 values for the slope m using the following relationship:

$$m = \frac{1}{N^{0.5}(n-1)} \sum_{i=1}^{n-1} \frac{R_g(T_{i+1}) - R_g(T_i)}{T_{i+1} - T_i}; \tag{4}$$

Here, N is the number of amino acids in each sequence, n is the number of replicas used in the simulation, and T_i is the temperature associated with replica i. The slope m was used to select 100 out of the 200 sequences that were chosen at random initially. The picking probability p was based on the following criterion:

$$p \propto \exp\left[-c\left(m - m_0\right)\right]; \tag{5}$$

Here, $c = 400$ in units that are reciprocal to m, and m_0 is set to -6.9×10^{-3} ÅK^{-1}. This choice enables efficient evolution of the GA and a strong selection for sequences with negative values of m. The parameter c ensures numerical stability, guarding against the unnormalized value of p becoming too large or too small.

The chosen parent sequences were used to generate 100 child sequences by mutating a single, randomly chosen position to a randomly chosen residue in the repeating unit. To avoid challenges with the prospect of introducing spurious disulfide bonds, we do not include Cys residues either in the original parent pool or for propagating the child sequences. The GA was

allowed to evolve for multiple iterations until the convergence criteria were met. These include the generation of at least 250 new sequences, each with a value of m being less than -5.0×10^{-3} ÅK^{-1}. For the results presented here, six iterations were sufficient to meet the prescribed convergence criteria. The picking probability p determines the selection pressure encoded into the GA. There needs to be an optimal balance between the two extremes in selection pressure. High selection pressures can lead to early convergence to a local optimum whereas low selection pressures can drastically slow down convergence [51]. The use of a single evolutionary operator can lead to a single sequence becoming the dominant choice. The number of iterations that pass before the emergence of a single sequence is known as the takeover time [51]. High selection pressures lead to low takeover times and vice versa. The issue of a single dominant individual emerging because less of a concern in sequence design given the high dimensionality of sequence space. We tuned the choice of c and m_0 to ensure that candidate sequences with putative UCST phase behavior can be part of the offspring, thus lending diversity to sequence evolution by the GA.

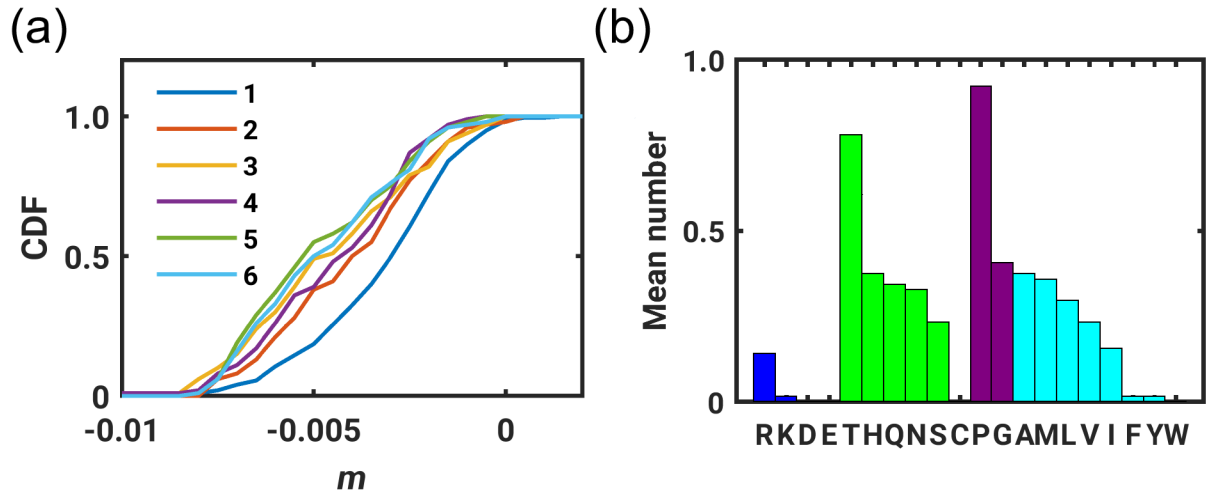

Figure 4. Calibration of the performance GA and statistics for compositional biases that emerge from application of the design protocol. (a) The cumulative distribution function (CDF) of the slope for sequences in each iteration. There is an overall shift for these CDFs towards the smaller m with each iteration of the GA. (b) The mean number of each residue in the 64 designed IDPs that are predicted to show LCST phase behavior. Residues in panel (b) are grouped into

categories based on their sidechain chemistries i.e., basic residues in blue bars, acidic residues in red bars (although these are not visible since they are not selected), polar residues in green, Pro and Gly in purple, and aliphatic as well as aromatic residues in cyan. Within each group, the bars are sorted in descending order of the mean numbers of occurrences in the designs.

Panel (a) in **Figure 4** quantifies the progress of the GA through each iteration of the design process. The quantification is performed in terms of cumulative distribution functions, which for each iteration will quantify the probability that the emerging sequences have associated slope values that are less than or equal to a specific value. The rightward shift in each iteration is indicative of the improved fitness vis-à-vis the selection criterion, which is the lowering of *m*.

As a final step in the sequence design, we added a post-processing step to increase the likelihood that the designed sequences are *bona fide* IDPs. Accordingly, we used the disorder predictor IUPRED2 [31] to quantify the disorder scores for each of the designed sequences. IUPRED2 yields a score between 0 and 1 for each residue, and only sequences where over half of the residues in the repeat are above 0.5 were selected as the final set of designs as sequences predicted to have LCST phase behavior. A particular concern with designing sequences for experimental prototyping is the issue of aggregation / precipitation. To ensure that designs were unlikely to create such problems, we calculated predicted solubility scores using the CamSol program [52] and found that all sequences that were selected after the post-processing step also have high solubility scores. This provides confidence that the designed IDPs are likely to show phase behavior via liquid-liquid phase separation above system-specific LCST values without creating problems of precipitation / aggregation.

Panel (b) in **Figure 4** summarizes the mean number of each amino acid type observed across the final tally of 64 designed sequences that survive the post-processing step. These statistics are largely in accord with the observations of Garcia Quiroz and Chilkoti [17]. Essentially

every sequence has at least once Pro residue in the repeat. The beta branched polar amino acid Thr is the other prominent feature that emerges from the selection. The remaining selection preferences fall into four distinct categories that include: (i) a clear preference for at least one polar amino acid *viz*., His, Ser, Thr, Asn, and Gln; (ii) a clear preference for the inclusion of at least one hydrophobic amino acid *viz*., Ala, Ile, Met, and Val; (iii) negligible selection, essentially an avoidance of the acidic residues Asp and Glu, as well as the aromatic residues Phe, Trp, and Tyr; and finally (iv) a preference for Arg over Lys, which is concordant with the distinct temperature dependent profiles for $\Delta\mu_h$ (**Figure 1**) and the large positive heat capacity of Arg, which is roughly three times larger than that of Lys (**Table 1**). Interestingly, if we fix the positions of Pro and Gly and select for residues in XPXXG or other types of motifs that are inspired by previous work on elastin-like polypeptides, the design process often converges on repeats that are known to be generators of polypeptides with *bona fide* LCST phase behavior (data not shown). This observation, and the statistics summarized in **Figure 4b** indicate that the design process uncovers sequences that are likely to have LCST phase behavior.

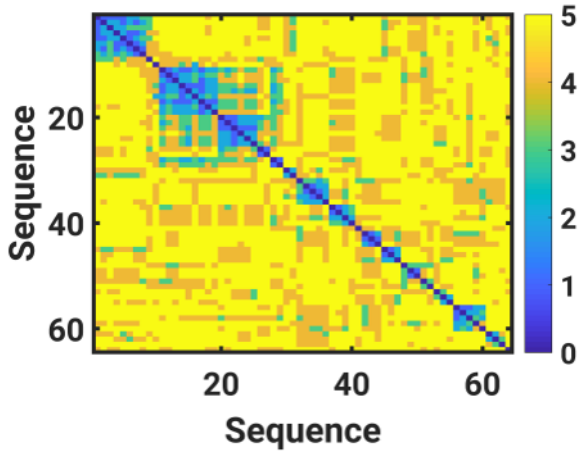

Figure 5. Identification of distinct sequence classes using a Hamming distance-based assessment of pairwise sequence similarities.

The designed sequences fall into distinct sequence classes: To quantify the degree of similarity among the set of designed sequences, we computed pairwise Hamming distances between all pairs of the 64 sequences. The resulting Hamming distances were then sorted, and sequences were clustered into distinct groups. Highly similar sequences have low Hamming distances, whereas the converse is true for dissimilar sequences. The resultant Hamming distance map is shown in **Figure 5**. The 64 sequences are unevenly distributed across nine major clusters. The actual sequences of the repeats, color-coded by their Hamming distance-based groupings, are shown in **Figure 6**. There are two features that stand out. First, sequences deviate from being repeats of VPGVG, which is the elastin-like motif. Second, we find that different sequence permutations on identical or similar composition manifolds emerge as candidates for LCST phase behavior. This observation suggests that at least in the IS limit it is the composition of each motif rather than the precise sequence that underlies adherence to the selection pressure in the GA. Interestingly, our observations are in accord with results from large-scale in vitro characterizations of sequences with LCST phase behavior [53]. These experiments show that composition, rather than the precise sequence, is a defining feature of LCST phase behavior – a feature that is distinct from sequences that show UCST phase behavior [3].

$(QPTGM)_{11}$	$(MTTGN)_{11}$	$(PTPLS)_{11}$	$(LTPSA)_{11}$	$(INSPH)_{11}$	$(AHQRI)_{11}$	$(SGNHM)_{11}$	$(VMRPG)_{11}$
$(GPTGM)_{11}$	$(PNKVV)_{11}$	$(QTPLS)_{11}$	$(LTGGQ)_{11}$	$(INAPH)_{11}$	$(VHNPP)_{11}$	$(HGNHM)_{11}$	$(VMPPQ)_{11}$
$(QPTGL)_{11}$	$(PTPLT)_{11}$	$(PAPLS)_{11}$	$(LNGGQ)_{11}$	$(ANAPH)_{11}$	$(MHNPP)_{11}$	$(PGTAT)_{11}$	$(VGRPM)_{11}$
$(QPTVM)_{11}$	$(PTNLT)_{11}$	$(LTPTQ)_{11}$	$(PTPQI)_{11}$	$(GNIPH)_{11}$	$(MQNPP)_{11}$	$(PHYAN)_{11}$	$(HMAPQ)_{11}$
$(TPTGM)_{11}$	$(PTNLS)_{11}$	$(LTPTT)_{11}$	$(PMPQI)_{11}$	$(RTAMT)_{11}$	$(GHTTL)_{11}$	$(QGHSA)_{11}$	$(TQIGH)_{11}$
$(TPTVM)_{11}$	$(PTPLV)_{11}$	$(LTPTA)_{11}$	$(APASS)_{11}$	$(RTAMG)_{11}$	$(GHRTL)_{11}$	$(NHMSA)_{11}$	$(TQQVH)_{11}$
$(GPTVM)_{11}$	$(PTPLA)_{11}$	$(LQPTA)_{11}$	$(APSSM)_{11}$	$(RTAPI)_{11}$	$(GHMTP)_{11}$	$(NHMVS)_{11}$	$(SFQNH)_{11}$
$(GPTVT)_{11}$	$(PNPLV)_{11}$	$(TTPTA)_{11}$	$(AHPPH)_{11}$	$(RTHAI)_{11}$	$(PGNIN)_{11}$	$(VMRPQ)_{11}$	$(QAGQT)_{11}$

Figure 6. Sequences of 64 designed IDPs that emerge from application of the GA. Different colors except black are used to label sequences in the same group.

ABSINTH-T simulations of coil-to-globule transitions for select sequences: We selected four sequence repeats *viz*., $(TPTGM)_{11}$, $(PTPLV)_{11}$, $(LTPTA)_{11}$, and $(RTAMG)_{11}$ for characterization using the full ABSINTH-T model and the calculation of phase diagrams. These sequences were chosen because they are representative from each of the four major classes that emerge from the design process. Additionally, these sequences bear minimal resemblance to extant designs or naturally occurring sequences that are known to have LCST phase behavior. Using all-atom, thermal replica exchange Monte Carlo simulations and the full ABSINTH-T model (see methods for details) we performed simulations to test for the presence of a collapse transition for each of the four sequences. The results are shown in **Figure 7**. All sequences show a clear tendency to form collapsed conformations as temperature increases. This is diagnosed by there being a clear preference for values of $R_gN^{0.5}$ being less than the theta state reference value of 2.5 at higher temperatures and values of $R_gN^{0.5}$ being greater than 2.5 at lower temperatures.

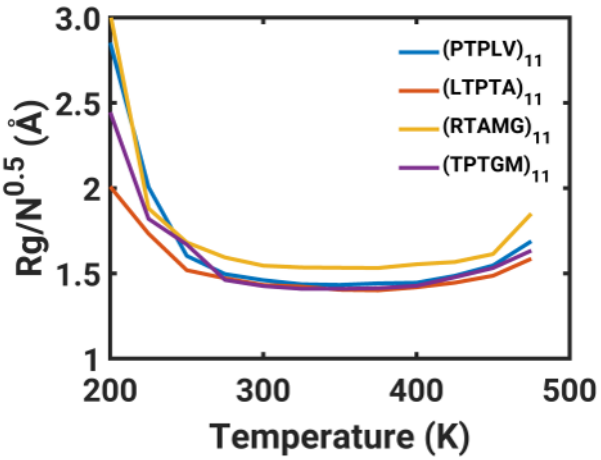

Figure 7. Profiles of normalized $R_gN^{0.5}$ vs. temperature for four IDPs designed using the GA. The results shown here use the full ABSINTH-T model. The theta temperatures extracted from these simulations are presented in the main text.

Analysis of coil-globule transitions, extraction of parameters, and calculation of phase diagrams using the Gaussian Cluster Theory: The profiles of $R_gN^{0.5}$ vs. T were analyzed to extract

the theta temperature (T_θ) for each of the four sequences. For this, we used a method that we described recently by Zeng et al., [28]. Only three of the four sequences have coil-globule transition profiles for which a robust estimate of the theta temperature can be made. The extent of expansion at low temperatures is modest and suggests that the apparent T_θ for $(LTPTA)_{11}$ is outside the window where converged simulations can be performed. For the other three sequences namely, $(PTPLV)_{11}$, $(RTAMG)_{11}$, and $(TPTGM)_{11}$, the estimated T_θ values are 210 K, 210 K, and 200 K, respectively.

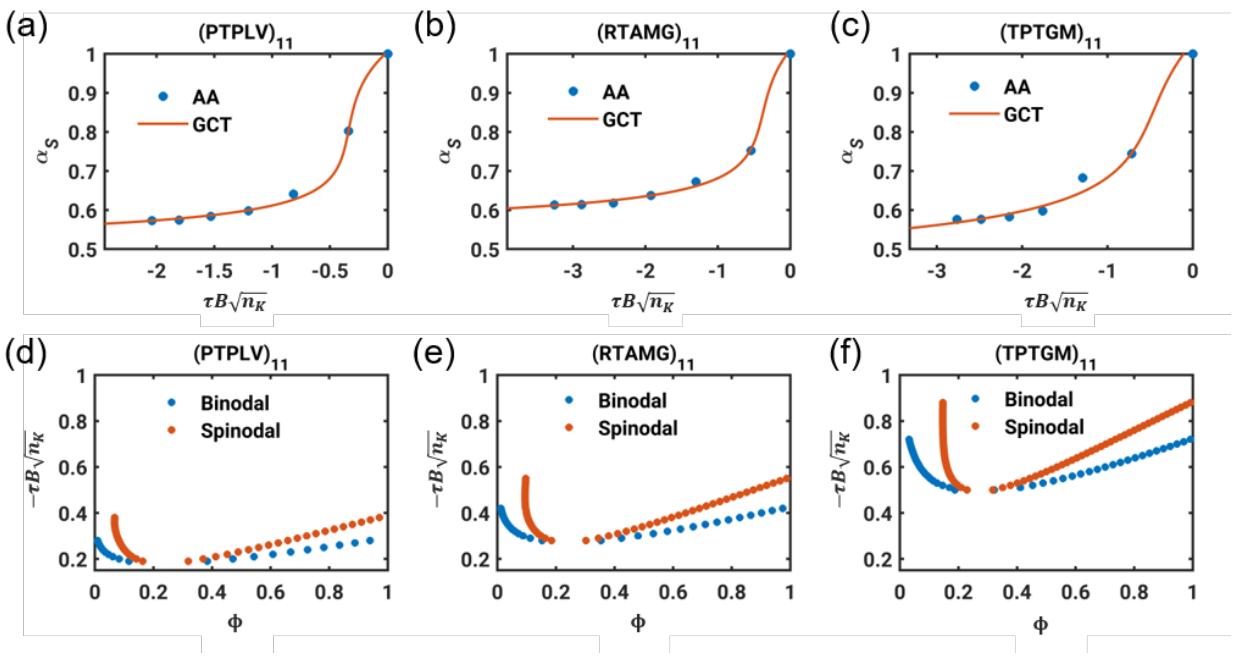

Figure 8. Results from application of the Gaussian Cluster Theory for calculating full phase diagrams. Panels (a-c) show the contraction ratio profiles for $(PTPLV)_{11}$, $(RTAMG)_{11}$ and $(TPTGM)_{11}$, respectively. Blue dots are the contraction ratio calculated from all atom simulations with ABSINTH-T at temperatures from 200 K to 350 K and red curves are fits to these data using the Gaussian Cluster Theory that lead to estimates of the sequence-specific values for the temperature dependent two-body interaction coefficient B and the temperature independent three-body interaction parameter w. Panels (d-f) show the full phase diagrams, including the binodal, spinodal, and the estimated location of the critical point for $(PTPLV)_{11}$, $(RTAMG)_{11}$ and $(TPTGM)_{11}$, respectively.

Next, we used the estimates of T_θ in conjunction with the Gaussian Cluster Theory of Raos and Allegra. We extracted the two and three-body interaction coefficients by fitting the contraction

ratio α_s calculated from simulations using the formalism of the Gaussian Cluster Theory and this yields sequence-specific estimates of B, the two-body interaction coefficient, and w, the three-body interaction coefficient (see panels (a) – (c) in **Figure 8**). These parameters were then deployed to compute full phase diagrams using the numerical approach developed by Zeng et al.,[28] and adapted by others [54]. The results are shown in panels (d) – (f) of Figure 8. The abscissae in these diagrams denote the bulk polymer volume fractions whereas the ordinates quantify temperature in terms of the thermal interaction parameter $-\tau B\sqrt{n_K}$. Here, $\tau = \left(\frac{T - T_\theta}{T_\theta}\right)$ which is positive for $T > T_\theta$, B is the temperature-dependent two-body interaction coefficient inferred from analysis of the contraction ratio, and n_K is the number of Kuhn segment in the single chain, which we set to be five. Note that B is negative for temperatures above T_θ. Accordingly, the thermal interaction parameter is positive above T_θ as well as the critical temperature T_c. Therefore, comparative assessments of the driving forces for LCST phase behavior can be gleaned by comparing the sequence-specific values of $-\tau B\sqrt{n_K}$ and the volume fraction at the critical point. It follows that the sequences can be arranged in descending order of the driving forces as $(TPTGM)_{11}$, $(RTAMG)_{11}$, and $(PTPLV)_{11}$, respectively. Importantly, full characterization of the phase behavior using a combination of all-atom simulations and numerical adaptation of the Gaussian Cluster Theory shows that, in general, sequences designed to have LCST phase behavior, do match the predictions (see **Figure 8**).

Discussion

In this work, we have adapted a GA to design novel sequences of repetitive IDPs that we predict to have LCST phase behavior. Our method is aided by a learned heuristic that was shown to provide clear segregation between sequences with known LCST vs. UCST phase behavior. This

heuristic is the slope m of the change in $R_gN^{0.5}$ vs. T from simulations of sequences performed in the IS limit of the ABSINTH-T model. We use the heuristic in conjunction with IS limit simulations to incorporate a selection pressure into the GA, thereby allowing the selection of sequences that are "fit" as assessed by the heuristic to be predictive of LCST phase behavior.

Here, we presented one instantiation of the GA and used it to uncover 64 novel sequences that can be grouped into four major classes and several minor classes (**Figure 6**). We then focused on four sequences, one each from each of the four major classes and characterized temperature dependent coil-globule transitions. These profiles, analyzed in conjunction with recent adaptations of the Gaussian Cluster Theory [32], allowed us to extract sequence-specific values for theta temperatures, temperature dependent values of the two body interaction coefficients, and three-body interaction coefficients. We incorporated these parameters into our numerical implementation [28] of the Gaussian Cluster Theory to calculate full phase diagrams for three sequences. These affirm the predictions of LCST phase behavior and the sequence-specificity in control over the driving forces for thermoresponsive phase behavior.

Our overall approach is aided by the following advances: We used the AMOEBA forcefield [29] to obtain direct estimates of temperature dependent free energies of solvation for model compounds used to mimic sidechain and backbone moieties. These temperature dependent free energies of solvation were used in conjunction with the integral of the Gibbs-Helmholtz equation to obtain model compound specific values for the enthalpy and heat capacity of hydration. The AMOEBA calculations represent the first direct estimates of temperature dependent hydration free energies using a polarizable forcefield, and they help circumvent many of the assumptions that have to be made in dissecting thermodynamic data for whole salts or protonated / deprotonated versions of acidic / basic groups in order to obtain experimentally derived estimates for

temperature independent [20] as well as temperature dependent μ_h values [19]. The only simplifications we make here are (a) the usage of the integral of Gibbs-Helmholtz equation to fit the temperature dependent μ_h values and (b) assuming that Δc_P is independent of temperature. To test the validity of these assumptions we will need to deploy novel BAR based estimators that allow us to quantify the temperature dependencies of enthalpies and entropies [55]. However, obtaining accurate estimates of the decompositions requires orders-of-magnitude more sampling as shown by Wyczalkowski et al., [55] and we will need to extract second moments of the enthalpies and entropies in order to obtain independent estimates of the temperature dependence of Δc_P.

The methods we present here are a start toward the integration of supervised learning to leverage information gleaned from systematic characterizations of IDP phase behavior and physical chemistry based computations that combined all-atom simulations with improvements such as ABSINTH-T, and theoretical calculations that allow us to connect single chain coil-globule transitions to full phase diagrams [28]. The heuristic we have extracted from IS limit simulations helps with discriminating sequences with LCST vs. UCST phase behavior. These simulations are sufficient for IS limit driven and GA aided designs of sequences that are expected to have LCST phase behavior. This is because composition as opposed to the syntactic details of sequences play a determining role of LCST phase behavior [3]. Recent studies have shown that even the simplest changes to sequence syntax can have profound impacts on UCST phase behavior [56]. This makes it challenging to guide the design of sequences with predicted UCST phase behavior that relies exclusively on IS limit simulations. One will need to incorporate simulations based on either transferrable [5757] or learned coarse-grained models [58] as a substitution for the IS limit simulations. This approach, although easy to articulate, comes with challenges because one has to be sure that the coarse-grained models afford the requisite sequence specificity without compromising

efficiency. The work of Dignon et al., [59] is noteworthy in this regard. Their coarse-grained model, which is based on knowledge-based potentials parameterized to have temperature-dependent interactions, have been shown to be very effective in discriminating sequences that are shown to have UCST versus LCST phase behavior [59]. The conceptual underpinnings of their approach and that presented here derive from the work of Wuttke et al.,[19] and in our case is further motivated by the physics of LCST phase behavior that has been articulated by Tanaka and colleagues. It would be interesting to combine or compare our approach to that of Dignon et al., in the context of designing novel IDPs and characterizing their phase behavior. We view these approaches as being complementary rather than competing ones and we expect that the approaches will have distinct advantages in different settings. The specific feature of our approach is that the calculations, at least for designing sequences with LCST phase behavior, do not ever become more complex than single chain simulations. This has value for achieving design objectives. It also has value for designing sequences that are not only thermoresponsive, but are also responsive to changes in pH, pressure, and other solvent parameters, especially since recent studies suggest that solution space scanning is a way to obtain efficient delineation of the desirable conformational and phase equilibria for IDPs [60].

The design of sequences with UCST phase behavior or sequences that combine UCST and LCST phase behavior, going beyond simple block copolymeric designs, will be of utmost interest for developing new IDP based materials. Additionally, we hope to build on improved understanding [61] of the impact of pH on conformational [62] and phase equilibria [63] of IDPs as well as the impact of metal chelation sites on phase behavior [64] to design sequences that combine the ability to exhibit phase behavior in response to orthogonal stimuli. Such efforts are of direct relevance to engineering orthogonal biomolecular condensates into simple unicellular prokaryotic

and eukaryotic cells, as has been demonstrated recently with the engineering a protein translation circuit into protocells based on a thermoresponsive elastin like polypeptide [65]. Of course, the proof of the validity / accuracy of designs and predictions will have to come from experimental work geared toward testing the predictions / designs. These efforts – that leverage high-throughput expression of these *de novo* sequences in *E. coli* and *in situ* characterization of their phase behavior – are underway [66]. Initial experimental investigations suggest that the designs reported here and those that will emerge from application of the methods deployed in this work do indeed show LCST phase behavior. Detailed reports of these experimental characterizations will follow in separate work.

Methods

AMOEBA forcefield parameterization for the model compounds of interest

To obtain values of free energies of solvation from AMOEBA simulations, we first derived the AMOEBA force field parameters for the model compounds listed in **Table 1** of the main text. The parameters for methane, methanol, ethanol, toluene and p-Cresol are taken from previous work [38], which is part of the amoeba09.prm parameter file in the released TINKER package [67]. The parameters for other model compounds are derived as follows. The AMOEBA potential energy function is composed of bonded and non-boned terms [29]. Bonded terms include bond stretching, angle bending, bond-angle stretch-bending coupling, out-of-plane bending, and torsional rotation. Non-bonded terms include van der Waals, permanent electrostatics and induced dipole polarization. The molecular structures were first fully optimized at MP2/6-31G* level of theory [68]. The molecular structures were first fully optimized at MP2/6-31G* level of theory. Force constant parameters for bonded interactions, van der Waals interactions, and polarizabilities were assigned from the existing Poltype library, and the equilibrium bonded values were from optimized

geometry. Based on the optimized geometry for each model compound, we performed single point energy calculations at the MP2/cc-pvtz level of theory to obtain compound specific electron densities. The initial multipole (charge, dipole and quadrupole) parameters were obtained from those electron densities by performing distributed multipole analysis calculation using GDMA program [69]. The atomic dipole and quadrupole moment parameters were further refined to reproduce the MP2/aug-cc-pvtz electrostatic potential (ESP). It is worth mentioning that harmonic restraint was applied to dipole and quadrupole in the ESP fitting, which is the new feature of the `potential` program in the TINKER software [67]. All the derived parameters involving bonded and non-bonded terms were then collected together. Finally, torsional parameters were obtained by comparing the conformational energy profile of quantum mechanical and AMOEBA based calculations. Along each torsional angle of the molecule, 12 conformers were generated. Torsion-restrained optimization was performed by employing HF method combining with 6-31G* basis set, followed by single point energy calculation using ωB97XD functional [70] with a larger basis function 6-311++G(d,p). All the quantum mechanics calculations were performed using the Gaussian 09 software package [71]. The parameterization procedure has been automated in the Poltype tool (https://github.com/pren/poltype/tree/poltype2).

Set up of molecular dynamics simulations using AMOEBA

All the AMOEBA simulations were performed using the TINKER-OpenMM package [72]. Each model compound was solvated in a cubic water box with periodic boundary conditions. The initial dimensions of the central cell were set to be 30×30×30 $Å^3$. Following energy minimization, molecular dynamics simulations were performed using integrators designed for the isothermal-isobaric ensemble (NPT) with the target temperature being between 273 and 400 K depending on the temperature of interest and the target pressure being 1 bar. Integrations of the equations of

motion were performed using the multiple time step RESPA integrator [73]. The temperature and pressure were controlled using a stochastic velocity rescaling thermostat [74] and a Monte Carlo constant pressure algorithm [75], respectively. The particle mesh Ewald method [76], with *B*-spline interpolation [77], with a real space cutoff of 7 Å was used to compute long-range corrections to electrostatic interactions. The cutoff for van der Waals interactions was set to be 12 Å. The integrating timestep is set to be 2.0 fs and coordinates are saved every 1.0 ps.

Free energy calculations

We used the BAR [37] method to quantify the free energies of solvation for the model compounds of interest. This method has been shown to be superior to other free energy estimators in terms of reducing the statistical errors in calculations of free energies of solvation [55]. The solute is grown in using two different Kirkwood coupling parameters *viz*., λ_{vdW} and λ_{el} that scale the strengths of solute-solute and solute-solvent van der Waals and electrostatic interactions. A series of independent molecular dynamics simulations were performed in the NPT ensemble for different combinations of λ_{vdW} and λ_{el}. We used the following combinations for the scaling coefficients: $[\lambda_{vdW}, \lambda_{el}]$ $\lambda \equiv$ [0, 0], [0.1, 0], [0.2, 0], [0.3, 0], [0.4, 0], [0.5, 0], [0.6, 0], [0.7, 0], [0.8, 0], [0.9, 0], [1, 0], [1, 0.1], [1, 0.2], [1, 0.3], [1, 0.4], [1, 0.5], [1, 0.6], [1, 0.7], [1, 0.8], [1, 0.9], [1, 1]. For each pair of λ values, we performed simulations, each of length 6 ns, at the desired temperature and a pressure of 1 bar. We then used TINKER `bar` program to calculate the free energy difference between neighboring windows defined in terms of the scaling coefficients. For every combination of λ_{vdW} and λ_{el}, we set aside the first 1 ns simulation as part of the equilibration process. Finally, for each model compound we computed free energies of solvation at six different temperatures viz., 275 K, 298 K, 323 K, 348 K, 373 K, 398 K, thus giving us the direct estimates of temperature dependent free energies of solvation that we sought from the AMOEBA based simulations.

The temperature dependent free energies of solvation were fit to the integral of the Gibbs-Helmholtz equation – see equation (1) in the main text. The free energy calculations provide us with direct estimates for rFoS(T) at specific values for T. We set T_0 = 298K and fit use non-linear regression to fit equation (1) to the calculated values for rFoS(T). The regression analysis provides estimates of ΔH and ΔC_P, which we then use, in conjunction with equation (1) in the manner prescribed by Wuttke et al.,[19] for all the ABSINTH-T based simulations.

Supporting Information

Please see supporting information for the sequences shown by Garcia Quiroz and Chilkoti to have UCST and LCST phase behavior that were used for IS limit simulations in this study.

Data Availability Statement

The data that support the findings in this study are available within the article and in the Supporting Information.

Acknowledgments

This work was supported by grants DMR 1729783 from the US National Science Foundation (AC, RVP), RGP0034/2017 from the Human Frontier Science Program (RVP), and R01GM114237 from the US National Institutes of Health (PR). Resources from the Center for High Performance Computing (CHPC) and the Research Infrastructure Services (RIS) at Washington University in St. Louis were used for some of the simulations.

References

1 Kiersten M. Ruff, Stefan Roberts, Ashutosh Chilkoti, and Rohit V. Pappu, Journal of Molecular Biology **430** (23), 4619 (2018).

[2] Marc S. Cortese, Vladimir N. Uversky, and A. Keith Dunker, Progress in Biophysics and Molecular Biology **98** (1), 85 (2008).

[3] M. Dzuricky, S. Roberts, and A. Chilkoti, Biochemistry **57** (17), 2405 (2018).

[4] Sarah Rauscher and Régis Pomès, in *Fuzziness: Structural Disorder in Protein Complexes*, edited by Monika Fuxreiter and Peter Tompa (Springer US, New York, NY, 2012), pp. 159.

[5] I. Weitzhandler, M. Dzuricky, I. Hoffmann, F. Garcia Quiroz, M. Gradzielski, and A. Chilkoti, Biomacromolecules **18** (8), 2419 (2017).

[6] J. R. Simon, N. J. Carroll, M. Rubinstein, A. Chilkoti, and G. P. Lopez, Nature chemistry **9** (6), 509 (2017).

[7] Merisa Saric and Thomas Scheibel, Current Opinion in Biotechnology **60**, 213 (2019).

[8] Jen Hsin, Johan Strümpfer, Eric H. Lee, and Klaus Schulten, Annual Review of Biophysics **40** (1), 187 (2011).

[9] Ruoxing Lei, Jessica P. Lee, Matthew B. Francis, and Sanjay Kumar, Biochemistry **57** (27), 4019 (2018).

[10] Anastasia K. Varanko, Jonathan C. Su, and Ashutosh Chilkoti, Annual Review of Biomedical Engineering **22** (1), 343 (2020).

[11] Juan J. de Pablo, Nicholas E. Jackson, Michael A. Webb, Long-Qing Chen, Joel E. Moore, Dane Morgan, Ryan Jacobs, Tresa Pollock, Darrell G. Schlom, Eric S. Toberer, James Analytis, Ismaila Dabo, Dean M. DeLongchamp, Gregory A. Fiete, Gregory M. Grason,

Geoffroy Hautier, Yifei Mo, Krishna Rajan, Evan J. Reed, Efrain Rodriguez, Vladan Stevanovic, Jin Suntivich, Katsuyo Thornton, and Ji-Cheng Zhao, npj Computational Materials **5** (1), 41 (2019).

12 R. K. Das, K. M. Ruff, and R. V. Pappu, Curr Opin Struct Biol **32**, 102 (2015).

13 Jordina Guillén-Boixet, Andrii Kopach, Alex S. Holehouse, Sina Wittmann, Marcus Jahnel, Raimund Schlüßler, Kyoohyun Kim, Irmela R. E. A. Trussina, Jie Wang, Daniel Mateju, Ina Poser, Shovamayee Maharana, Martine Ruer-Gruß, Doris Richter, Xiaojie Zhang, Young-Tae Chang, Jochen Guck, Alf Honigmann, Julia Mahamid, Anthony A. Hyman, Rohit V. Pappu, Simon Alberti, and Titus M. Franzmann, Cell **181** (2), 346 (2020).

14 Jeong-Mo Choi, Alex S. Holehouse, and Rohit V. Pappu, Annual Review of Biophysics **49** (1), 107 (2020).

15 Sudeep Banjade, Qiong Wu, Anuradha Mittal, William B. Peeples, Rohit V. Pappu, and Michael K. Rosen, Proceedings of the National Academy of Sciences **112** (47), E6426 (2015).

16 Megan C. Cohan and Rohit V. Pappu, Trends in Biochemical Sciences **45** (8), 668 (2020).

17 F. Garcia Quiroz and A. Chilkoti, Nature Materials **14** (11), 1164 (2015).

18 Fumihiko Tanaka, Tsuyoshi Koga , Isamu Kaneda, and Françoise M. Winnik, Journal of Physics: Condensed Matter **23** (28), 284105 (2011).

19 R. Wuttke, H. Hofmann, D. Nettels, M. B. Borgia, J. Mittal, R. B. Best, and B. Schuler, Proc Natl Acad Sci U S A **111** (14), 5213 (2014).

[20] A. Vitalis and R. V. Pappu, J Comput Chem **30** (5), 673 (2009).

[21] Tyler S. Harmon, Michael D. Crabtree, Sarah L. Shammas, Ammon E. Posey, Jane Clarke, and Rohit V. Pappu, Protein Engineering, Design and Selection **29** (9), 339 (2016).

[22] Hiroyuki Kojima, Polymer Journal **50** (6), 411 (2018).

[23] Guangzhao Zhang and Chi Wu, Advances in Polymer Science **195**, 101 (2006).

[24] B. H. Zimm and J. K. Bragg, The Journal of Chemical Physics **31** (2), 526 (1959).

[25] Yukinori Okada and Fumihiko Tanaka, Macromolecules **38** (10), 4465 (2005).

[26] Hiroyuki Kojima and Fumihiko Tanaka, Macromolecules **43** (11), 5103 (2010).

[27] Fumihiko Tanaka, Macromolecules **33** (11), 4249 (2000).

[28] Xiangze Zeng, Alex S. Holehouse, Ashutosh Chilkoti, Tanja Mittag, and Rohit V. Pappu, Biophysical Journal **119** (2), 402 (2020).

[29] Jay W. Ponder, Chuanjie Wu, Pengyu Ren, Vijay S. Pande, John D. Chodera, Michael J. Schnieders, Imran Haque, David L. Mobley, Daniel S. Lambrecht, Robert A. DiStasio, Martin Head-Gordon, Gary N. I. Clark, Margaret E. Johnson, and Teresa Head-Gordon, The Journal of Physical Chemistry B **114** (8), 2549 (2010).

[30] R. K. Das and R. V. Pappu, Proc Natl Acad Sci U S A **110** (33), 13392 (2013).

[31] Bálint Mészáros, Gábor Erdős, and Zsuzsanna Dosztányi, Nucleic Acids Research **46** (W1), W329 (2018).

[32] Guido Raos and Giuseppe Allegra, The Journal of chemical physics **104** (4), 1626 (1996).

[33] Themis Lazaridis and Martin Karplus, Proteins: Structure, Function, and Bioinformatics **35** (2), 133 (1999).

[34] Aditya Radhakrishnan, Andreas Vitalis, Albert H. Mao, Adam T. Steffen, and Rohit V. Pappu, The Journal of Physical Chemistry B **116** (23), 6862 (2012).

[35] George I. Makhatadze, Maria M. Lopez, and Peter L. Privalov, Biophysical Chemistry **64** (1), 93 (1997).

[36] Ninad V. Prabhu and Kim A. Sharp, Annual Review of Physical Chemistry **56** (1), 521 (2005).

[37] Charles H. Bennett, Journal of Computational Physics **22** (2), 245 (1976).

[38] Pengyu Ren, Chuanjie Wu, and Jay W. Ponder, Journal of Chemical Theory and Computation **7** (10), 3143 (2011).

[39] Alan Grossfield, Pengyu Ren, and Jay W. Ponder, Journal of the American Chemical Society **125** (50), 15671 (2003).

[40] Yue Shi, Chuanjie Wu, Jay W. Ponder, and Pengyu Ren, Journal of Computational Chemistry **32** (5), 967 (2011).

[41] Charlotte S. Sørensen and Magnus Kjaergaard, Proceedings of the National Academy of Sciences **116** (46), 23124 (2019).

[42] Rachel S. Fisher and Shana Elbaum-Garfinkle, Nature Communications **11** (1), 4628 (2020).

[43] Jie Wang, Jeong-Mo Choi, Alex S Holehouse, X Zhang, M Jahnel, R Lemaitre, S Maharana, A Pozniakovsky, D Drechsel, I Poser, Rohit V Pappu, Simon Alberti, and Anthony A Hyman, Cell **174**, 688 (2018).

[44] Jamie A. Greig, Tu Anh Nguyen, Michelle Lee, Alex S. Holehouse, Ammon E. Posey, Rohit V. Pappu, and Gregory Jedd, Molecular Cell **77** (6), 1237 (2020).

[45] Masahiro Kinoshita and Takashi Yoshidome, The Journal of Chemical Physics **130** (14), 144705 (2009).

[46] Jeong-Mo Choi and Rohit V. Pappu, Journal of Chemical Theory and Computation **15** (2), 1367 (2019).

[47] A. D. MacKerell, D. Bashford, M. Bellott, R. L. Dunbrack, J. D. Evanseck, M. J. Field, S. Fischer, J. Gao, H. Guo, S. Ha, D. Joseph-McCarthy, L. Kuchnir, K. Kuczera, F. T. K. Lau, C. Mattos, S. Michnick, T. Ngo, D. T. Nguyen, B. Prodhom, W. E. Reiher, B. Roux, M. Schlenkrich, J. C. Smith, R. Stote, J. Straub, M. Watanabe, J. Wiórkiewicz-Kuczera, D. Yin, and M. Karplus, The Journal of Physical Chemistry B **102** (18), 3586 (1998).

[48] George A. Kaminski, Richard A. Friesner, Julian Tirado-Rives, and William L. Jorgensen, The Journal of Physical Chemistry B **105** (28), 6474 (2001).

[49] Lucas Sawle, Jonathan Huihui, and Kingshuk Ghosh, Journal of Chemical Theory and Computation **13** (10), 5065 (2017).

[50] Ayori Mitsutake, Yuji Sugita, and Yuko Okamoto, The Journal of Chemical Physics **118** (14), 6664 (2003).

[51] Matthew P. Thompson, Jeff D. Hamann, and John Sessions, International Journal of Forestry Research **2009**, 527392 (2009).

[52] Pietro Sormanni and Michele Vendruscolo, Cold Spring Harbor Perspectives in Biology **11** (12) (2019).

[53] Miriam Amiram, Felipe Garcia Quiroz, Daniel J. Callahan, and Ashutosh Chilkoti, Nature Materials **10** (2), 141 (2011).

[54] Han-Yi Chou and Aleksei Aksimentiev, The Journal of Physical Chemistry Letters **11** (12), 4923 (2020).

[55] Matthew A. Wyczalkowski, Andreas Vitalis, and Rohit V. Pappu, The Journal of Physical Chemistry B **114** (24), 8166 (2010).

[56] Felipe Garcia Quiroz, Nan K. Li, Stefan Roberts, Patrick Weber, Michael Dzuricky, Isaac Weitzhandler, Yaroslava G. Yingling, and Ashutosh Chilkoti, Science Advances **5** (10), eaax5177 (2019).

[57] Z. Monahan, V. H. Ryan, A. M. Janke, K. A. Burke, S. N. Rhoads, G. H. Zerze, R. O'Meally, G. L. Dignon, A. E. Conicella, W. Zheng, R. B. Best, R. N. Cole, J. Mittal, F. Shewmaker, and N. L. Fawzi, EMBO J **36** (20), 2951 (2017).

[58] Jeong-Mo Choi, Furqan Dar, and Rohit V. Pappu, PLOS Computational Biology **15** (10), e1007028 (2019).

[59] Gregory L. Dignon, Wenwei Zheng, Young C. Kim, and Jeetain Mittal, ACS Central Science **5** (5), 821 (2019).

[60] Alex S. Holehouse and Shahar Sukenik, Journal of Chemical Theory and Computation **16** (3), 1794 (2020).

[61] Felipe Garcia Quiroz, Vincent F. Fiore, John Levorse, Lisa Polak, Ellen Wong, H. Amalia Pasolli, and Elaine Fuchs, Science **367** (6483), eaax9554 (2020).

[62] Martin J. Fossat and Rohit V. Pappu, The Journal of Physical Chemistry B **123** (32), 6952 (2019).

[63] Omar Adame-Arana, Christoph A. Weber, Vasily Zaburdaev, Jacques Prost, and Frank Jülicher, Biophysical Journal **119** (8), 1590 (2020).

[64] Kibeom Hong, Daesun Song, and Yongwon Jung, Nature Communications **11** (1), 5554 (2020).

[65] Joseph R. Simon, Seyed Ali Eghtesadi, Michael Dzuricky, Lingchong You, and Ashutosh Chilkoti, Molecular Cell **75** (1), 66 (2019).

[66] Michael Dzuricky, Bradley A. Rogers, Abdulla Shahid, Paul S. Cremer, and Ashutosh Chilkoti, Nature chemistry **12** (9), 814 (2020).

[67] Joshua A. Rackers, Zhi Wang, Chao Lu, Marie L. Laury, Louis Lagardère, Michael J. Schnieders, Jean-Philip Piquemal, Pengyu Ren, and Jay W. Ponder, Journal of Chemical Theory and Computation **14** (10), 5273 (2018).

[68] Thom H. Dunning Jr., The Journal of Chemical Physics **90** (2), 1007 (1989).

[69] Anthony J. Stone, Journal of Chemical Theory and Computation **1** (6), 1128 (2005).

[70] Jeng-Da Chai and Martin Head-Gordon, The Journal of Chemical Physics **128** (8), 084106 (2008).

[71] G. W. Trucks M. J. Frisch, H. B. Schlegel, G. E. Scuseria, M. A. Robb, J. R. Cheeseman, G. Scalmani, V. Barone, B. Mennucci, G. A. Petersson, H. Nakatsuji, M. Caricato, X. Li, H. P. Hratchian, A. F. Izmaylov, J. Bloino, G. Zheng, J. L. Sonnenberg, M. Hada, M. Ehara, K. Toyota, R. Fukuda, J. Hasegawa, M. Ishida, T. Nakajima, Y. Honda, O. Kitao, H. Nakai, T. Vreven, J. A. Montgomery, Jr., J. E. Peralta, F. Ogliaro, M. Bearpark, J. J. Heyd, E. Brothers, K. N. Kudin, V. N. Staroverov, R. Kobayashi, J. Normand, K. Raghavachari, A. Rendell, J. C. Burant, S. S. Iyengar, J. Tomasi, M. Cossi, N. Rega, J. M. Millam, M. Klene, J. E. Knox, J. B. Cross, V. Bakken, C. Adamo, J. Jaramillo, R. Gomperts, R. E. Stratmann, O. Yazyev, A. J. Austin, R. Cammi, C. Pomelli, J. W. Ochterski, R. L. Martin, K. Morokuma, V. G. Zakrzewski, G. A. Voth, P. Salvador, J. J. Dannenberg, S. Dapprich, A. D. Daniels, Ö. Farkas, J. B. Foresman, J. V. Ortiz, J. Cioslowski, and D. J. Fox, G09: Gaussian (Gaussian Inc., Wallingford CT, 2009).

[72] Matthew Harger, Daniel Li, Zhi Wang, Kevin Dalby, Louis Lagardère, Jean-Philip Piquemal, Jay Ponder, and Pengyu Ren, Journal of Computational Chemistry **38** (23), 2047 (2017).

[73] Mark E. Tuckerman, Bruce J. Berne, and Glenn J. Martyna, The Journal of Chemical Physics **94** (10), 6811 (1991).

[74] Giovanni Bussi, Tatyana Zykova-Timan, and Michele Parrinello, The Journal of Chemical Physics **130** (7), 074101 (2009).

[75] Johan Åqvist, Petra Wennerström, Martin Nervall, Sinisa Bjelic, and Bjørn O. Brandsdal, Chemical Physics Letters **384** (4), 288 (2004).

[76] Tom Darden, Darrin York, and Lee Pedersen, The Journal of Chemical Physics **98** (12), 10089 (1993).

[77] Ulrich Essmann, Lalith Perera, Max L. Berkowitz, Tom Darden, Hsing Lee, and Lee G. Pedersen, The Journal of Chemical Physics **103** (19), 8577 (1995).